The Nonlinear Behaviour of Generic Tail Fins for Small Wind Turbines

Amr A. Khedr,[1] Mohamed M. Hammam,[2] Abhineet Gupta,[3] Emmanuel Branlard,[4] Francesco Castellani,[1] and David H. Wood[5]

[1)]*Department of Engineering, University of Perugia, Via Duranti, Perugia, 06125, Italy*

[2)]*Department of Mechanical Power Engineering, Faculty of Engineering, Port Said University, Port Said, Port Fuad, 42526, Egypt*

[3)]*National Renewable Energy Laboratory, 19001 W 119th Ave, Arvada, Colorado,80007, USA*

[4)], *Department of Mechanical and Industrial Engineering, University of Massachusetts Amherst, 160 Governors Dr., Amherst, Massachusetts, 01003, USA*

[5)]*Department of Mechanical and Manufaturing Engineering, University of Calgary, 2500 University Dr., Calgary T2N 1N4, Canada*

(*Electronic mail: dhwood@ucalgary.ca)

(Dated: 26 August 2024)

This paper describes analysis and measurements of the yaw response of tail fins for small wind turbines. It is based on an extension of unsteady slender body theory (USBT) to cover non-slender fins and high angles of incidence, both of which make the theory nonlinear. We provide three main additions to the substantial literature on linearized USBT for tail fins. First, USBT is extended to high angles by modeling the nonlinear vortex dynamics. Second, the restriction to slender bodies is removed by modeling the chordwise load variation. Third, we consider the effect of time-varying wind speed. The extended theory is compared to wind tunnel measurements of the yaw behaviour of delta, elliptical, and rectangular tail fins without a rotor and nacelle. The fins were released from initial yaw angles of -40° and -80°; the latter is of sufficient magnitude to show the importance of the nonlinear yaw dynamics. Generally good agreement was found between the theory and measurements, and the theory was shown to be more accurate than a "polar" or quasi-steady model which uses only the lift and drag of a delta planform. Of the three planforms, the rectangular one showed the lowest accuracy in terms of frequency but the damping was accurately predicted. Overall, the results demonstrate the importance of nonlinearity in the response of a yawing tail fin, particularly for the higher aspect ratio fins at large yaw angles.

I. INTRODUCTION

Small wind turbines (SWTs) with a power output less than about 20 kW often use a tail fin to align the rotor with the wind, whereas all large turbines have a motorized yaw drive. The "passive" system on SWTs is much cheaper, but comes with a price: it may not be easy to limit the yaw rate about the tower, which can lead to high gyroscopic loads. Despite the importance of a well-designed tail fin for efficient and safe SWT operation, the aeroelastic modeling of tail fins is not well developed. As an example of the situation, the well-known aeroelastic software OpenFAST and its predecessors[1] has had a simple quasi-steady tail fin module since Version 7, released in 2002. That module uses a look-up table of tail fin lift and drag to determine the forces and moments. A major aim of this work is to provide an unsteady and nonlinear theory for a new tail fin module for OpenFAST. Clearly, the theory had to be implementable in OpenFAST which limited it to two possible forms, the first being the quasi-steady one just described. The alternative developed here models the response as a nonlinear ordinary differential equation in the yaw angle whose constants are determined analytically or experimentally for any tail fin planform.

It follows from the requirements of this work that computational fluid dynamics (CFD) simulations of pitching airfoils and various planforms, e.g. Carta, Putzu, and Ghisu[2], Hammer, Garmann, and Visbal[3], are of limited value, especially as the range of yaw angles studied in these and similar references, is much smaller than those considered here. We believe that CFD for wider ranges of yaw angles and planforms other than the generic ones studied here, will become valuable in the future development of yaw response models.

There are several rules-of-thumb for tail fin design, but very little data on their behaviour, Bradney, Evans, and Clausen[4], and no well-established engineering guidelines for the design of tail fins. The yaw response of generic tail fin planforms in the absence of a rotor and nacelle was measured in a wind tunnel by Singh, Hemmati, and Wood[5] for a single wind speed and low release angle. By characterizing the response in terms of the damping ratio and natural frequency, they found that a delta wing is a representative planform for tail fins. Since a delta wing of low aspect ratio was used to develop unsteady slender body theory (USBT) for tail fins, Bradney, Evans, and Clausen[4], Singh, Hemmati, and Wood[5], Wood[6], it is the basis for the present analysis. The other generic planforms we consider are ellipses and rectangles. For all three planforms, flow separation is critical in determining the aerodynamic forces and moments at high incidence, but we show below that it is reasonable to ignore Reynolds number effects. Further, these generic planforms can have a wide range of aspect ratio, defined for any planform as $AR = b_0^2/S$ where b_0 is the span, and S the area. Figure 1 shows the geometry of delta and elliptical fins. USBT by definition is restricted to low AR and its extension to higher AR leads to nonlinear moment equations that are similar in form but with different constants for the three planforms, so the yaw response cannot be simply categorized by a damping ratio and natural frequency. The elliptical tail was selected partly because the USBT potential

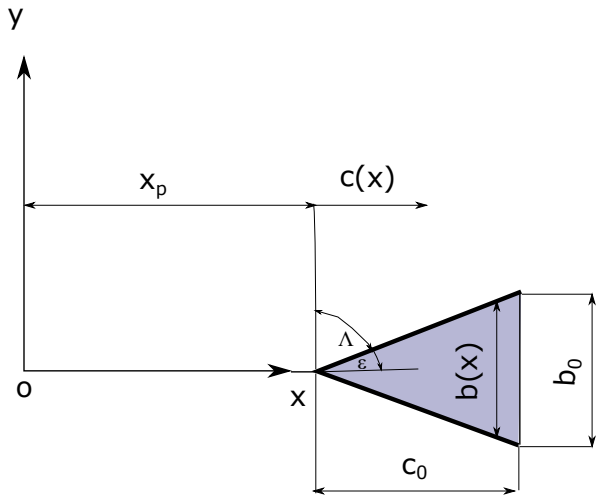

(a) A delta tail fin.

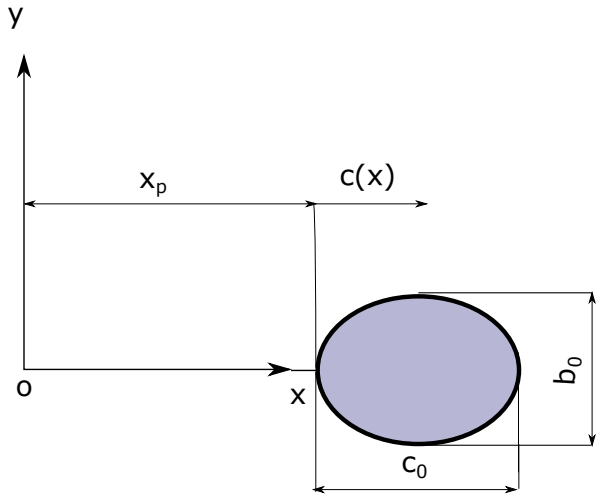

(b) An elliptic tail fin.

FIG. 1: Tail fin planforms.

loads, which dominate at low incidence, are generated only on that part of the fin where $b(x)$, the fin leading edge in fig. 1(a), is increasing or constant. Thus, the back half of an elliptical tail fin serves no purpose for the linear aerodynamics. This important practical aspect of the theory is tested herein.

A tail fin is most needed for turbine starting. When subjected to a wind gust, an initially stationary rotor may have its axis at a large yaw angle, γ, to the wind, Wood[6]. One scenario for large γ is the following. If the turbine centre of mass is not aligned with the tower axis and the tower is not vertical, then the stationary turbine will have a preferred orientation which can be at any γ. Tail fins also help to reduce γ during power production which is important because a yaw error reduces the output power by a factor of approximately $\cos^2\gamma$, Wood[6]. Yaw alignment also relates to the gyroscopic bending moments on the blades and main shaft. Their magnitude depends on the product of blade inertia, blade angular velocity, and yaw rate relative to a fixed observer. They can be the major ultimate loads on a SWT, Wood[6], and can also contribute significantly to the fatigue loads, Evans *et al.*[7].

For small γ, USBT reduces to a linear, second order differential equation, e.g. Bradney, Evans, and Clausen[4], Singh, Hemmati, and Wood[5], Wood[6], which is very similar to that used for the modeling of wind vanes for wind direction measurement, e.g. Kerhascoët *et al.*[8]. Linearized modeling also requires that the angle of attack of the tail fin, α, is equal to γ, which, in turn, requires $r\dot{\gamma}/U \ll 1$, where the dot denotes a time derivative, r is tail boom reference length, and U is the wind speed. This inequality holds at high U, partly because typical values of $\dot{\gamma}$ for wind turbines decrease with increasing U, Bradney, Evans, and Clausen[4], probably because of the stabilizing effect of the power-producing rotor, which is not considered here. Thus, the inequality is most often violated when a SWT is starting. Hammam and Wood[9] extended USBT to high γ by including the nonlinear dependence on γ and separating the representation of α from that of γ. This leads to both lift and drag causing yaw moments about the tower axis. Because of the length of the report by Hammam and Wood[9], the detailed development of the equations will not be reproduced; the interested reader can consult the publically-available reference.

Here we present the full moment equations for the generic planforms of delta wings, ellipses, and rectangles, give a summary of their derivation, and compare them to wind tunnel tests made in the absence of a rotor and nacelle. As in Singh, Hemmati, and Wood[5], the tail fins were yawed to an initial yaw angle, γ_0, and released. The subsequent $\gamma(t)$ was measured and compared to the theory. It is recognized that the low-turbulence of a wind tunnel, with a constant or known variation of wind speed, is a significant abstraction from the reality of SWT operation. Further, atmospheric turbulence levels tend to increase with decreasing wind speed, e.g. Wood[6], and we anticipate that the yaw model is most important for SWT starting at low speed. On the other hand, the controlled environment should allow a comparative testing of generic planforms and an assessment of the basic suitability of the yaw model. This needs to be followed by field tests of SWTs to validate the model in the harsher real environment.

The major novelty of the present experiments was to use γ_0 of -40° and $-80°$, that is, large enough in magnitude to show the nonlinear effects, and to undertake the measurements at a range of wind speeds, U, to test the theory's scaling of the yaw response and the significance of Reynolds number. Tests were done also for a time-varying U, but $\dot{U}$ could not be made large enough to determine the importance of its effects.

The next section provides a summary of the analysis in Hammam and Wood[9] and presents the full moment equations. Section 3 describes the wind tunnel experiments. It is followed by the presentation of the results and comparison to USBT. The delta fin results are also compared to the polar model used in OpenFAST. Section 5 considers modifications to the theory and the final section summarizes the investigation and gives the conclusions.

II. THE MOMENT EQUATIONS FOR GENERIC TAIL FINS

Here we summarize the equations derived in Hammam and Wood [9] and explain the origin of the various terms The analysis ignores any aerodynamic effects of the tail boom.

A. Delta tail fins

The response equations are obtained from integrating the general dynamic response equation, (5.2) of Hammam and Wood [9], for the particular tail fin planform. Equation (8.2) of [9] gives the moment equation for a delta fin as

$$\begin{aligned}
M_z = I_z\ddot{\gamma} = &-0.5\rho A_{tf} \\
&\times \left[\left\{\left(\frac{3}{5}-\frac{1}{2}\sin\varepsilon\right)c_0^3+\left(\frac{3}{2}-\frac{6}{5}\sin\varepsilon\right)x_p c_0^2\right.\right. \\
&\left.\left.+\left(1-\frac{3}{4}\sin\varepsilon\right)x_p^2 c_0\right\}\frac{K_p}{3-2\sin\varepsilon}\ddot{\gamma}+Ux_1\cos\gamma\right. \\
&\times\left\{\frac{3}{5}\left(\frac{5-4\sin\varepsilon}{3-2\sin\varepsilon}\right)c_0^2+\frac{3}{2}\left(\frac{4-3\sin\varepsilon}{3-2\sin\varepsilon}\right)x_p c_0+x_p^2\right\}K_p\dot{\gamma} \\
&+U^2x_1\cos\gamma(x_p+x_{cp}c_0)K_p\sin\gamma+\left\{\left(\frac{3}{4}-\frac{3}{5}\sin\varepsilon\right){c_0}^2\right. \\
&\left.+\left(1-\frac{3}{4}\sin\varepsilon\right)x_p c_0\right\}\frac{K_p}{3-2\sin\varepsilon}\dot{U}\sin\gamma\Big] \\
&-0.5\rho A_{tf}\left[2U\sin\gamma\left(\frac{1}{2}c_0^2+\frac{4}{3}x_p c_0+x_p^2\right)\dot{\gamma}\right. \\
&\left.+\left(\frac{2}{5}c_0^3+\frac{3}{2}x_p c_0^2+2x_p^2 c_0+x_p^3\right)\dot{\gamma}^2+\left(x_p+\frac{2c_0}{3}\right)U^2\sin^2\gamma\right] \\
&\times\left(x_2K_v+(1-x_3)C_{Dc}\right)\mathrm{sign}(U\sin\gamma+r\dot{\gamma}) \qquad (1)
\end{aligned}$$

where the terms involving K_p, the potential flow coefficient, unify its low- and high$-AR$ representation. K_v is the vortex lift coefficient, which was introduced by Polhamus [10]. C_{Dc} is the drag coefficient when the fin is normal to the flow. I_z is the total moment of the tail fin and tail boom around the yaw-axis and origin for x in Fig. 1, $r \approx x_p + c_0$, and ρ the density of air. The tail boom length, x_p, and maximum chord, c_0, are defined in Fig. 1. The angle ε is related to the sweep angle, Λ, by $\varepsilon = \pi/2 - \Lambda$ as shown in Figure 1, and to AR by $\tan\varepsilon = b_0/(2c_0) = AR/4$. Dots continue to denote time derivatives. The center of pressure, x_{cp} of delta wing is

$$x_{cp} = 1 - \frac{1-\sin\varepsilon/2}{3-2\sin\varepsilon} \qquad (2)$$

as a fraction of c_0.

Equation (1) is formatted to show the linearizable terms in $\dot{\gamma}$ and $\ddot{\gamma}$, containing K_p but not K_v, in the second to the fourth lines. On the fifth line is the steady term due to potential flow, which is linearized when $\cos\gamma \approx 1$ and $\sin\gamma \approx \gamma$. The remainder of the fifth line and the sixth, is the unsteady wind speed term, which can also be linearized. It is considered in Section IV D. K_p, which dominates at low γ, depends only on the planform. USBT gives the normal force N, and its coefficient, C_N, as

$$C_N = \frac{4N}{\rho U^2 b_0 c_0} = \frac{\pi AR}{2}\cos\gamma\sin\gamma. \qquad (3)$$

so that $K_p = \pi AR/2$ for delta wings of small AR; note that small AR is strictly required for USBT to be valid. Equation (4.5) of Hammam and Wood [9] gives K_p at high AR, that is, non-zero ε, from Traub [11] as

$$K_p = \frac{\pi AR}{2}\left(1-\frac{2}{3}\sin\varepsilon\right) = \frac{\pi AR}{2}\left(1-\frac{2AR}{3\sqrt{4+AR^2}}\right). \qquad (4)$$

The difference from the low$-AR$ results, as well as the correction to x_{cp} in Eq. (2) involving $\sin\varepsilon$, comes from the assumption of linear chordwise loading over the tail fin rather than the constant loading assumed in USBT. Similarly, for K_v:

$$K_v = \frac{\pi AR}{2\sin\varepsilon}\left(1-\frac{2}{3}\sin\varepsilon\right)\left(\frac{1}{2}+\frac{1}{3}\sin\varepsilon\right). \qquad (5)$$

The nonlinear vortex terms involving K_v are in the last three lines. K_v is bounded by $\pi \le K_v \le 3.45$ for $0 \le AR \le 4$ for a straight-edged delta wing, Polhamus [10]. All our delta fin simulations used $K_v = \pi$. The terms involving x_i, for $i = \{1,2,3\}$ scale the normal forces to give the contribution of the three force components: potential flow, K_p, vortex flow and break down, vortex burst, K_v, and full separation, C_{Dc}, Jouannet and Krus [12]. The more general form of the normal force equation (3) is

$$\begin{aligned}
C_N = &\, x_1 K_p \cos\gamma\sin\gamma + x_2 K_v|\sin\gamma|\sin\gamma \\
&+ (1-x_3)C_{Dc}\,|\sin\gamma|\sin\gamma \qquad (6)
\end{aligned}$$

where the first term comes from (3) and is the only one that becomes linear as $|\gamma| \to 0$. C_{Dc} depends on AR but Hammam and Wood [9] suggest a general value of 1.3 can be used.

The $x_i,\ i = \{1,2,3\}$, are called "separation functions" that satisfy $0 \le x_i \le 1\ \forall\ i$. They depend on γ and $\dot{\gamma}$, All three x_i are modeled by a first order differential equation of common form, Goman and Khrabrov [13]:

$$\tau_1\frac{\partial x_i}{\partial t} + x_i = x_{i,0}(\gamma - \tau_2\dot{\gamma}) \qquad (7)$$

where $\tau_1 \simeq 8c_0/U, \tau_2 \simeq 0.5c_0/U$ are time constants, and $i = \{1,2,3\}$. $\dot{\gamma} \simeq \dot{\gamma}$ is the pitch rate, and $x_{i,0}(\gamma - \tau_2\dot{\gamma})$ means that each $x_{i,0}$ is a function of $(\gamma - \tau_2\dot{\gamma})$ that decays exponentially as in Fan and Lutze [14]:

$$x_{i,0}(\gamma - \tau_2\dot{\gamma}) = \left(1+\exp[\sigma(\gamma - \tau_2\dot{\gamma} - \gamma_i^*)]\right)^{-1} \qquad (8)$$

where σ is an empirical constant that expresses the rate of decay of the forcing function. The characteristic time c_0/U is very small for a tail fin so $\tau_2\dot{\gamma}$ can be neglected, and γ replaced by $|\gamma|$. Thus

$$x_{i,0}(\gamma - \tau_2\dot{\gamma}) \approx x_{i,0}(\gamma) = \left(1+\exp[\sigma(|\gamma| - \gamma_i^*)]\right)^{-1} \qquad (9)$$

where γ_i^* can have different values for each flow component. For potential flow, it is the stall angle, and for vortex flow, it is the angle of attack at which the vortex from the tail fin apex bursts. At this angle, the separation function $x_i = 0.5$, as can be seen from Eq. (7) and (8). All response calculations presented herein used Eq. (9) with $\tau_2 = 0$.

Jouannet and Krus [15] recommended that γ_1^* be the angle at which the vortex breaks down at the trailing edge and $\gamma_2^* = \gamma_3^*$ be the γ at which the vortex breaks down at the wing apex. Jouannet and Krus [15] give the transition constants σ to be between 0.2 and 0.4. It was found, however, that $\sigma_1 = 0.3$ and $\sigma_2 = 0.1$ are good choices for most delta wings with $\sigma_3 \leq \sigma_2$. γ_1^* and γ_2^* could be obtained from Fig. 1 of Lowson and Riley [16] that shows the regions of fully separated flow and flow with no vortex breakdown, as a function of angle of attack and sweep angle for a delta wing. Setting γ_1^* to be the stall angle at each Λ, however, was found to give better results.

Hammam and Wood [9] analyzed experimental data to arrive at $\sigma_1 = 0.3$ and $\sigma_2 = \sigma_3 = 0.1$. $\alpha_1^* = 39^\circ$ and $\alpha_2^* = \alpha_3^* = 60^\circ$, where α_1^* is the stall angle while α_2^* and α_3^* are the angle at which the vortex breaks from the apex, and $C_{Dc} = 1.3$.

B. Elliptical tail fins

This section presents the yaw moment equation for an elliptic tail fin shown in Fig. 1b. An ellipse, or indeed any planform where $b(x)$ goes smoothly to zero at the trailing edge, is surprisingly difficult to accommodate in USBT. The reason is that only the front half of the ellipse (from $b(x) = 0$ to $b(x) = c_0/2$) will generate potential force and moments. However, the leading edge vortex exerts a pressure over the full elliptical section giving $K_v \approx \pi$ for all ARs from wind tunnel experiments, Okamoto and Azuma [17]. It was assumed in Hammam and Wood [9] that the force distribution over the ellipse surface is linear with the chord, $c(x)$. Also the high-AR correction has the same form used for the delta fin, namely, as a function of $\sin\varepsilon$.

With a similar, small correction to the A_{tf} term, Equation (8.4) of Hammam and Wood [9] gives the moment equation as

$$
\begin{aligned}
I_z\ddot{\gamma} &= -0.5\rho A_{tf} \\
&\times \left[\left\{\left(\frac{9}{80} - \frac{7}{80}\sin\varepsilon\right)c_0^3 + \left(\frac{5}{8} - \frac{9}{20}\sin\varepsilon\right)x_p c_0^2 \right.\right. \\
&\left.\left. + \frac{1}{8}(8 - 5\sin\varepsilon)x_p^2 c_0\right\}\frac{K_p}{3-\sin\varepsilon}\ddot{\gamma} + Ux_1\cos\gamma \right. \\
&\times \left\{\frac{1}{40}\left(\frac{30-21\sin\varepsilon}{3-\sin\varepsilon}\right)c_0^2 + \frac{1}{4}\left(\frac{12-7\sin\varepsilon}{3-\sin\varepsilon}\right)x_p c_0 + x_p^2\right\}K_p\dot{\gamma} \\
&+ U^2 x_1\cos\gamma(x_p + x_{cp}c_0)K_p\sin\gamma + \left\{\left(\frac{5}{16} - \frac{9}{40}\sin\varepsilon\right){c_0}^2\right. \\
&\left.\left. + \left(1 - \frac{5}{8}\sin\varepsilon\right)x_p c_0\right\}\frac{K_p}{3-\sin\varepsilon}\dot{U}\sin\gamma\right] \\
&- 0.5\rho A_{tf}\left[2U\sin\gamma\left(\frac{5}{16}c_0^2 + x_p c_0 + x_p^2\right)\dot{\gamma}\right. \\
&\left. + \left(\frac{7}{32}c_0^3 + \frac{15}{16}x_p c_0^2 + \frac{3}{2}x_p^2 c_0 + x_p^3\right)\dot{\gamma}^2 + \left(x_p + \frac{c_0}{2}\right)U^2\sin^2\gamma\right] \\
&\times \left(x_2 K_v + (1-x_3)C_{Dc}\right)\mathrm{sign}(U\sin\gamma + r\dot{\gamma}) \qquad (10)
\end{aligned}
$$

which has the same form as (1) for delta fins, which we have emphasized by placing the similar terms on the same rows of Eq.s (1) and (10). $x_{cp} = 1/6$ for low AR, but moves forward with increasing AR, asymptoting to $x_{cp} = 0.28$ for infinite AR, Krienes [18]. A simple fit to the x_{cp} data in Krienes [18] gives

$$x_{cp} = 0.12(2.35 - \exp(-0.94AR)). \qquad (11)$$

$K_p = \pi AR/2$ and $AR = 4b_0/(\pi c_0)$ for an elliptical wing. Because of the lack of data for the separation angles α_i^* for $i = \{1,2,3\}$, the values for an ellipse are based on those of a delta planform of the same AR. Equation (6.2) of Hammam and Wood [9] gives the general form of K_p for an elliptical tail fin as

$$K_p = \pi AR(1 - 2\sin\varepsilon/3). \qquad (12)$$

ε for the ellipse was also assumed to be that for the delta planform of the same AR, so that $\sin\varepsilon = AR/\sqrt{4+AR^2}$. For an example of the values used, we describe below the testing of a low $AR = 0.50$ which is equivalent to $\Lambda = 82^\circ$. $\alpha_1^* = 38^\circ$, while $\alpha_2^* = 55^\circ$ and $\alpha_3^* = 60^\circ$. It is also assumed that the σs are the same as for a delta fin because no values have been measured or computed for elliptical planforms.

C. Rectangular tail fins

In calculating the vortex force and moments acting on a rectangular tail fin, the leading edge and side edges are treated separately. When $c_0/x_p \ll 1$, however, the vortex flow over a rectangular fin can be approximated as that over a delta tail fin of the same dimensions. This combines the effect of the two edge vortices and consequently simplifies the model without compromising the accuracy. The vortex moment of a rectangular tail fin is assumed to be that of a delta tail fin having the

same c_0 and b_0 .

Lomax and Sluder [19] derived a correction function for chordwise loads over delta and rectangular wings of low aspect ratios. This function, however, can only be integrated numerically. As an alternative, we re-use the assumption made for the delta and elliptical planforms: the loading is linear with chord. This linear distribution is scaled with an AR term that vanishes as $AR \downarrow 0$, and is then used to derive the high AR corrections. For the steady state term, a relation for K_p for a rectangular planform that fits the analysis in Lomax and Sluder [19] was derived by Helmbold [20] and restated in many references, for instance, Lamar [21], as

$$K_p = \frac{2\pi AR}{2+\sqrt{AR^2+4}}. \tag{13}$$

and $AR = b_0/c_0$. The dynamic equation for a rectangular tail fin from Hammam and Wood [9] Eq. (8.6) is

$$\begin{aligned}
I_z\ddot{\gamma} &= -0.5\rho A_{tf} \\
&\times \left[\left\{\left(\frac{1}{3}-\frac{1}{4}\sin\varepsilon\right)c_0^3+\left(1-\frac{2}{3}\sin\varepsilon\right)x_p c_0^2\right.\right. \\
&\left.\left.+\left(1-\frac{1}{2}\sin\varepsilon\right)x_p^2 c_0\right\}K_p\ddot{\gamma}+Ux_1\cos\gamma\right. \\
&\times\left\{\left(1-\frac{2}{3}\sin\varepsilon\right)c_0^2+(2-\sin\varepsilon)x_p c_0+x_p^2\right\}K_p\dot{\gamma} \\
&+U^2x_1\cos\gamma(x_p+x_{cp}c_0)K_p\sin\gamma+\left\{\left(\frac{1}{2}-\frac{1}{3}\sin\varepsilon\right)c_0{}^2\right. \\
&\left.+\left(1-\frac{1}{2}\sin\varepsilon\right)x_p c_0\right\}K_p\dot{U}\sin\gamma\Big] \\
&-0.5\rho A_{tf}\left[2U\sin\gamma\left(\frac{1}{3}c_0^2+x_p c_0+x_p^2\right)\dot{\gamma}\right. \\
&\left.+\left(\frac{1}{4}c_0^3+x_p c_0^2+\frac{3}{2}x_p^2 c_0+x_p^3\right)\dot{\gamma}^2+\left(x_p+\frac{c_0}{2}\right)U^2\sin^2\gamma\right] \\
&\times\left(x_2K_v+(1-x_3)C_{Dc}\right)\mathrm{sign}(U\sin\gamma+r\dot{\gamma})
\end{aligned} \tag{14}$$

Each row in (14) corresponds to the same row in Eq. (1). ε is taken to be the value for a delta planform that is circumscribed by the rectangular one. K_v now receives a contribution from the leading edge, $K_{v,le}$, and the side edges, $K_{v,se}$, such that $K_v = K_{v,le} + K_{v,se}$. For $AR = 0.5$, $K_{v,se} = 2.5$ and $K_{v,le} = 0.4$, Lamar [21]. For an equivalent delta wing of $AR = 0.5$, $\alpha_1^* = 39^\circ$ from Okamoto and Azuma [17] while $\alpha_2^* = 55^\circ$, $\alpha_3^* = 60^\circ$ as determined in Hammam and Wood [9]. $K_p = \pi AR/2$ for a rectangular tail fin for small AR from Eq. (13), and x_{cp} moves downwind with increasing AR, which is the same direction as for swept wings, Hopkins [22], but the opposite direction for a delta fin. $x_{cp} \to 0.25$ as AR increases. From Lomax and Sluder [19], the dependence of x_{cp} is given by

$$x_{cp} = 0.25\left[1-\exp(-AR)\right]. \tag{15}$$

For the high $AR = 2$ rectangular tail fin, we used the α_i^* for the high$-AR$ = 1.97 delta wing of $\alpha_1^* = 33^\circ$, $\alpha_2^* = 38^\circ$, and $\alpha_3^* = 38^\circ$. $K_{v,se} = 1.57$, and $K_{v,le} = 1.5$ from Lamar [21].

The nonlinear ordinary differential equations for all three planforms were solved in the same way. NDSolve in Mathematica was used without changing its default accuracy.

III. EXPERIMENTAL METHODS

The tests were carried out in the return circuit/open test chamber wind tunnel "R. Balli" at Perugia University in Italy, Fig. 2. The air is accelerated through a contraction and exits through a square outlet 2.2×2.2 m into the working section, and is recovered through a diffuser with an inlet of 2.7×2.7 m which allows the flow to slow down before entering the curved ducts. The wind flow is generated with a fan with 11 carbon fiber blades driven by a 375 kW electric motor that can produce a speed of 47 m/s in the working section, and is controlled by an inverter that gives the options of constant wind speed, wind ramp control or a sine wave speed with a specified mean value and amplitude. More details about the wind tunnel and its ramp option can be found in Castellani *et al.* [23]. Honeycomb upstream of the test section guarantees a low turbulence intensity flow at the working section inlet, about 0.41% and 0.52% at a wind speed of 10 and 20 m/s respectively. Two Pitot-static tubes are fixed at the inlet of the test section to measure the wind speed. Temperature and humidity sensors inside the test section give the air density during the tests. The tunnel control room is located in front of the test chamber and isolated, for safety reasons, by a reinforced glass window. All the sensors used are wired to a data logger which in turn is connected to the control room where the data are processed using LABVIEW software.

All tail fin tests used a vertical tower with a fixed base centered on a small freely rotating shaft mounted by two bearings and housing a shaft encoder to measure the yaw angle. A horizontal circular rod formed the tail boom, which was attached to the vertical shaft at its highest point. Two holes were drilled at the end of the horizontal axis to attach different tail fins using two screws. To set γ_0, a manual mechanism comprising a blocking part and a releasing rope was installed at the top of the vertical column, Figs. 3 and 4. The releasing mechanism allowed the setting of the required γ_0 with the help of the encoder reading. Figure 3 shows a schematic of the tail fin test setup inside the wind tunnel in illustrating the different components of the setup and the tunnel, as well as the control and procedure of the tests.

Measurements were conducted by yawing the horizontal arm to a specific γ_0, then holding it in place. As soon as the wind speed stabilized, the mechanism was manually released using the attached thin rope, allowing the model to yaw freely on its pivot until it reached an equilibrium position. During this movement, the encoder readings were collected through the data logger and sent to a PC with LABVIEW software that saved the time history data along with the test conditions at a sampling rate of 1000 Hz. No smoothing or filtering was applied to the data. A limited number of experiments were repeated. For the high AR delta fin at 10 m/s with $\gamma_0 = -45^\circ$, the second experiment gave an r.m.s. difference from the first of 0.43° over the full response time of 9.4 s. The r.m.s. dif-

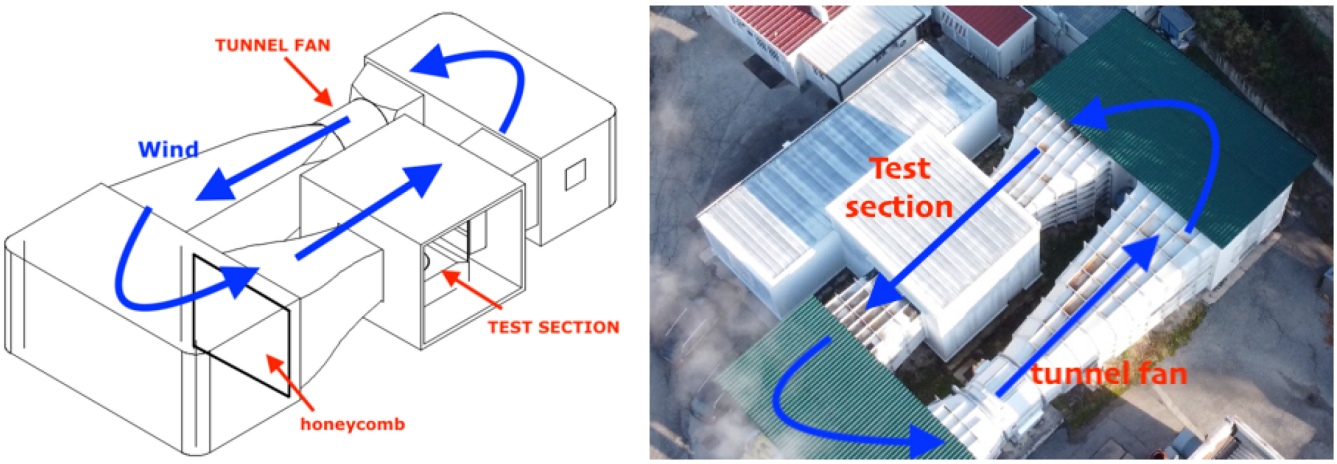

FIG. 2: Raffaele Balli wind tunnel at Perugia University.

ferences for 1 s subsets of the full data were not significantly different from that value.

Planform	AR	c_0 (m)	b_0 (m)	I_z (kgm^2)
delta	0.58	0.27	0.078	0.0473
elliptical	0.5	0.18	0.070	0.0367
rectangular	0.5	0.143	0.072	0.0359
delta	1.97	0.143	0.141	0.0376
elliptical	1.74	0.095	0.130	0.0327
rectangular	2.03	0.07	0.142	0.0323

TABLE I: Geometry of the tail fins. $x_p = 0.443$ m for all fins.

The tail fins used in the experiments were flat, zero camber plates made of 3 mm aluminium with sharp square edges. Table I provides the geometry of these tail fins and the two delta fins are shown in Fig. 4. Two values of γ_0 were used in this study; -40°, and -80° relative to the direction of air flow, with clockwise being positive. All the models were tested at three wind speeds; 5, 10, and 17 m/s. The delta fin is also studied under unsteady wind speed (sine wave) with a mean value of 9.86 m/s, 1.5 m/s amplitude, 120° phase angle, and a frequency of 0.63 rad/s.

IV. RESULTS

This Section presents the results for the tail fins listed in Table I. The first three rows document the low AR fins which will be discussed first as they are supposedly easier to model. All the experimental yaw responses have the superficial form of a second order linear system, so we will continue to use the terms "frequency" and "damping" as qualitative indicators. Likewise, the use of negative γ_0 is to maintain consistency with the experiments, so the terms "high" and "low" γ will refer to their magnitudes.

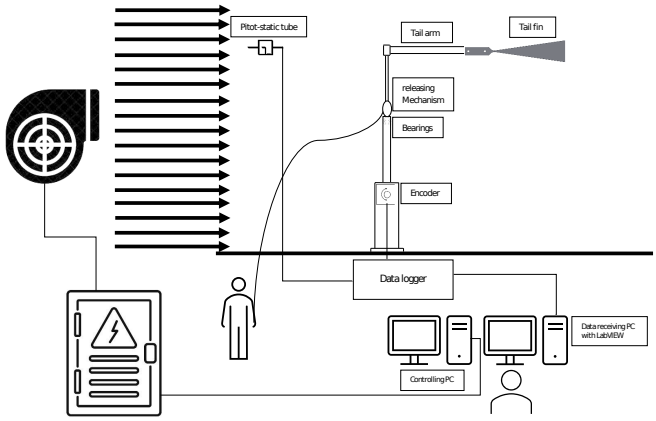

FIG. 3: Schematic diagram of the tail fin test inside the wind tunnel.

Planform	K_p	K_v	x_{cp}	$\alpha_1^*(^\circ)$	$\alpha_2^*(^\circ)$	$\alpha_3^*(^\circ)$
delta	0.911	π	0.667	39	60	60
elliptical	0.778	π	0.206	38	55	60
rectangular	0.785	2.9	0.098	39	55	60
delta	2.184	π	0.625	33	38	38
elliptical	2.373	π	0.258	33	38	38
rectangular	2.630	π	0.217	33	38	38

TABLE II: Model constants. $C_{Dc} = 1.3, \sigma_1 = 0.3$, and $\sigma_2 = \sigma_3 = 0.1$ for all fins. Note that x_{cp} is given as a fraction of c_0. Note that x_i for $i = \{1,2,3\}$ are given by Eqs. (7) and (9).

A. The importance of nonlinearity

In view of the complexity of the nonlinear yaw equations and what was just noted about the apparent linearity of the measured yaw responses, we first establish the importance of the nonlinearity. This should be most apparent at large yaw and high aspect ratios, so Fig. 5 compares the measured re-

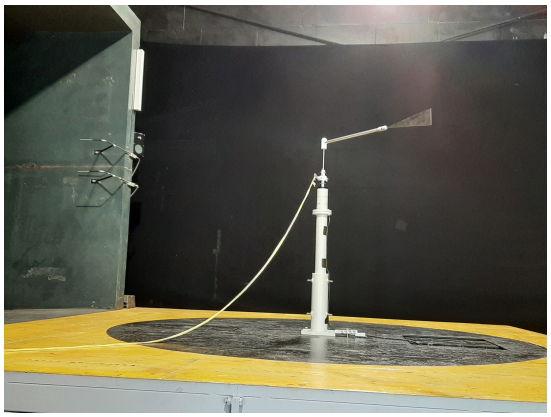

(a) Low aspect ratio delta fin.

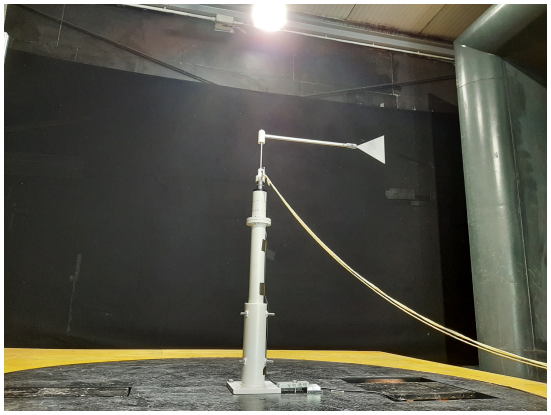

(b) High aspect ratio delta fin.

FIG. 4: The two delta tail fins used in this study.

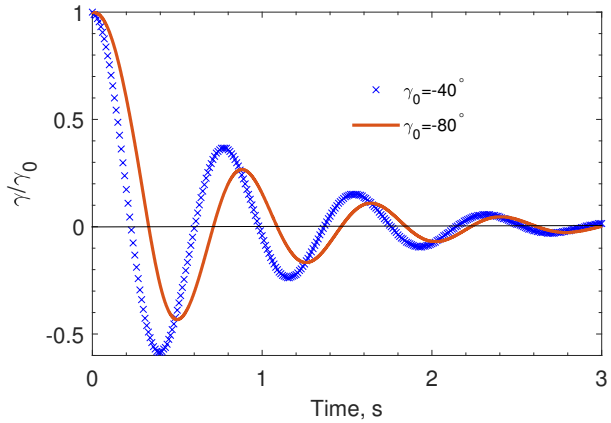

(a) Full response for $\gamma_0 = -40°$ and $-80°$.

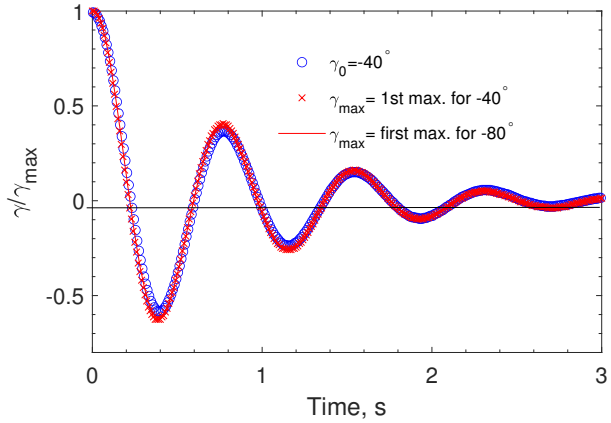

(b) Response rescaled by γ_{max}, the first maxima in $\gamma(t) = 46.82°$ and $17.3°$ for $\gamma_0 = -40°$ and $-80°$ respectively. Time on the $x-$axis is $t - t_{max}$.

FIG. 5: Comparison of the yaw response of a delta tail fin of $AR = 1.97$ for the two release angles. $U = 17$ m/s.

sponse of the highest AR delta fin for the two release angles, in terms of $\gamma(t)/\gamma_0$ against time, t. Only every tenth experimental data point for $\gamma_0 = -40°$ is plotted to allow for easy comparison. If the two responses were governed by the same linear equation, this scaling would collapse the two responses, which is clearly not the case in Part (a). What is most noticeable is that the time of the first zero crossing is considerably smaller for $\gamma_0 = -40°$, after which the frequency of the response is approximately independent of γ_0. This is made clearer in Part (b) where the responses are rescaled by γ_{max}, the first maxima in $\gamma(t)$; $\gamma_{max} = 46.82°$ at $t_{max} = 0.493$ s and $17.30°$ at $t_{max} = 0.389$ s for $\gamma_0 = -80°$ and $-40°$ respectively, and the $x-$axis shows $t - t_{max}$. The results now collapse, showing the nonlinear terms in the moment equations are needed for $\gamma(t)$ higher than about $45°$. We do not show any further results of rescaling in the interests of brevity, but resetting γ_{max} to subsequent local maxima for each γ_0 gives a collapse in γ/γ_{max} similar to that shown in Part (b).

Two other perspectives on the nonlinearity of the model response are available: the first comes from the plot of the separation functions in Fig. 6, also for the highest AR delta fin at the largest γ_0. The solid lines show the separation functions determined with $\tau_2 = 0$ and the dashed lines are for $\tau_2 = 0.5c_0/U$. The difference is generally small enough to

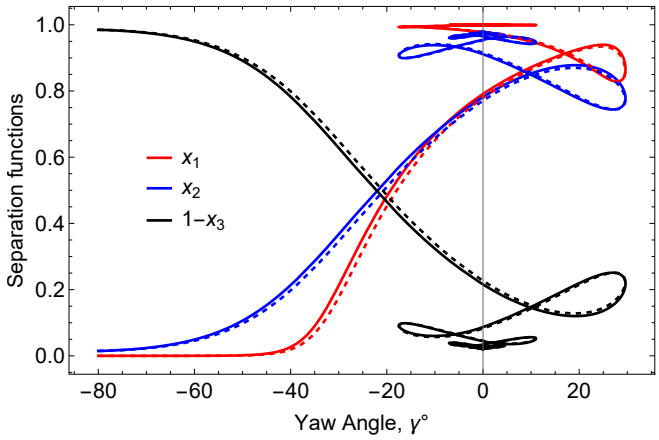

FIG. 6: The separation functions for the delta tail fin of $AR = 1.97$ for $\gamma_0 = -80°$ and $U = 17$ m/s. x_1 is shown in red, x_2 in blue, and $1 - x_3$ in black. The solid lines were computed for $\tau_2 = 0$ as used in the rest of the paper. The dashed lines show non-zero τ_2.

justify the neglect of τ_2 for the following simulations. The nonlinear x_3 is most important immediately following release, followed by the nonlinear x_2. As $|\gamma|$ decreases, the linearizable x_1 increases but never dominates, showing that there is no clear division between nonlinear and linear response. Second, analysis of the nonlinear equation in Hammam and Wood[24] showed that the deviation of the nonlinear from the linear solution is positive for angles greater than 45° and negative (as well as smaller in magnitude) at lower angles. The multiple values of the separation function for $|\gamma| \lesssim 20°$ reflect the hysteresis in the tail fin lift and drag that are routinely encountered in experiments on pitching delta wings and other planforms. The time-dependence of the separation functions was introduced to provide that behaviour.

B. Low aspect ratios

The simplest test of the model is a comparison of the predictions with the steady wind tunnel experiments for the delta fin at low $AR = 0.58$. The test conditions were $U = 17$ m/s, and $\gamma_0 = -40°$. Part (a) of Fig. 7 shows good agreement between the measurements and Eq. (1) with the damping slightly over-predicted. Part (b) contains only experimental results taken at wind speeds of 17, 10, and 5 m/s, with t normalized by U/x_p. This normalization collapses the results except for over-estimating the damping at $U = 5$ m/s. Hammam and Wood[9] attribute this to the increasing importance of bearing friction; the aerodynamic moments depend on U^2 and so overwhelm the frictional torque at the two higher speeds. No further results for $U = 5$ m/s will be presented. In the absence of bearing friction, the frequency of the response is proportional to U, an important result for tail fin design and operation. Further, the results imply that Reynolds number effects are not important as was assumed in developing the theory.

Predictions and measurements for the delta fin at higher $\gamma_0 = -80°$ are compared in Fig. 8. The agreement is as good as for the lower γ_0 in Fig. 7(a).

The predictions for the low AR delta tail fin using the quasi-steady (polar) model in OpenFAST are shown in blue in Figs. 7(a) and 8, taken from Gupta *et al.*[25]. The current model gives better prediction of the damping and frequency compared to the polar one. Also, it is noted that polar model application requires the lift and drag for the corresponding planform and AR over a wide range of γ, which are available for this delta planform but not for the elliptical case.

The yaw response of an elliptical tail fin of low $AR = 0.50$ is compared to the measurements for $\gamma_0 = -40°$ and $-80°$ in Fig. 9. For $\gamma_0 = -40°$ and $U = 10$ m/s, the results are shown in Part (a), and in Part (b) for $U = 17$ m/s and (high) $\gamma_0 = -80°$. The accuracy of the model at high γ_0, which increases the nonlinearity of the response, is comparable to that at $\gamma_0 = -40°$.

Figure 10 for the rectangular fins, shows the largest errors that we found for the current model. It significantly underestimates the frequency while capturing the damping in the measurements. The uncertainty in the α^*s and σs is likely to be the main cause of the disagreement, judging by the im-

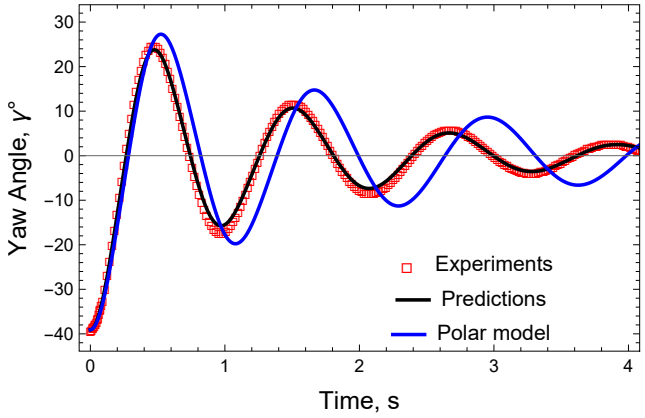

(a) Yaw angle predictions (black line) compared to the measurements (□), and polar model (blue line). $U = 17$ m/s.

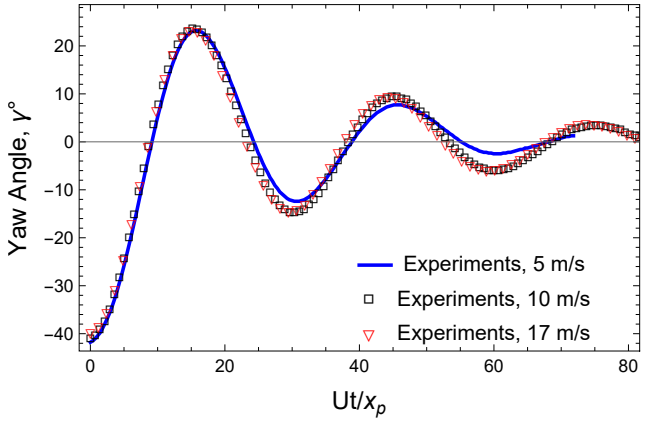

(b) Measured responses against Ut/x_p for 17 m/s (∇), 10 m.s, □, and 5 m/s (blue line).

FIG. 7: Yaw response of a delta tail fin of $AR = 0.58$, and $\gamma_0 = -40°$.

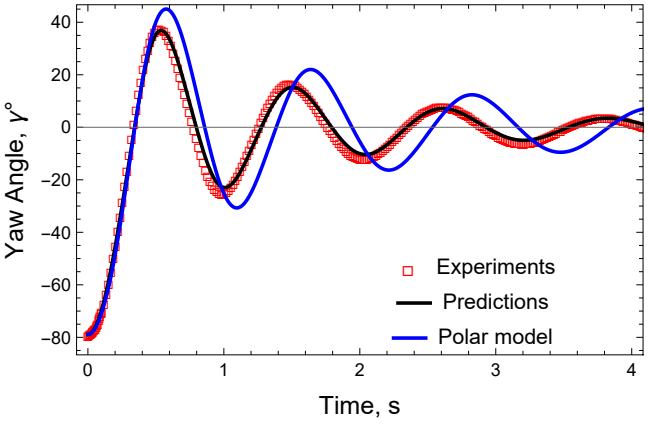

FIG. 8: Yaw angle predictions (black line) compared to the experimental results (□) , and polar model (blue line) for a delta wing tail fin of $AR = 0.58, U = 17$ m/s and $\gamma_0 = -80°$.

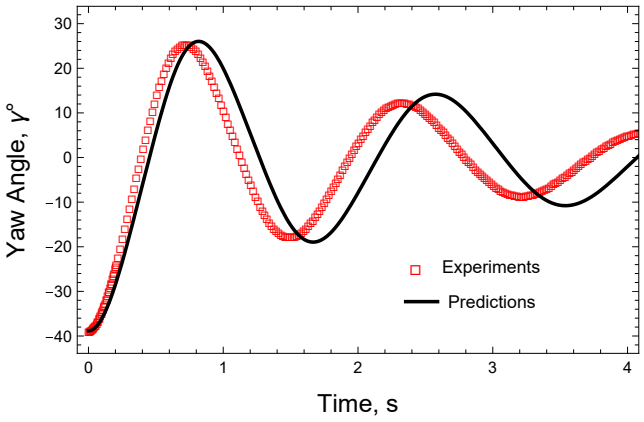

(a) $U = 10$ m/s and $\gamma_0 = -40°$.

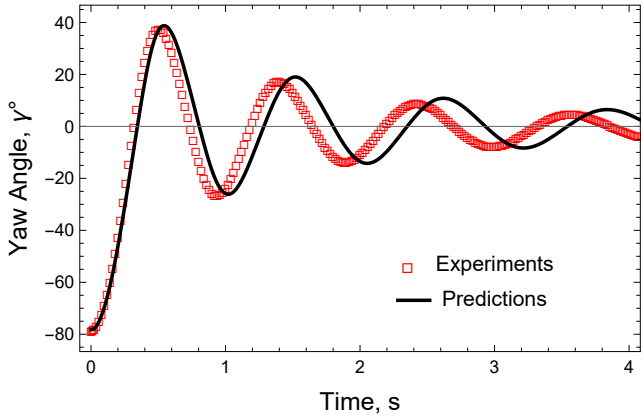

(b) $U = 17$ m/s and $\gamma_0 = -80°$.

FIG. 9: Yaw angle predictions of an elliptic tail fin (black line) compared to the experimental results (□). $AR = 0.50$.

proved agreement obtained using system identification techniques to optimize the values, while the other values in in Table II were kept unaltered, Hammam and Wood[9].

C. High aspect ratios

In this section, the theory for $AR > 1$ is validated against experiments at $U = 17$ m/s for all three planform/s, and the same two values of γ_0. The delta fin results are shown in Fig. 11(a) for $\gamma_0 = -40°$ and in Part (b) for the higher $\gamma_0 = -80°$. The theory is, surprisingly, of similar accuracy for the two values of γ_0, implying that the modeling of the nonlinear effects at high γ is acceptable.

Figure 12 shows the comparison for elliptic tail fin of $AR = 1.74$. The predictions are not as close as for the low AR fin in Fig. 9 with the discrepancy in both the frequency and damping of the response. Nevertheless, the agreement is sufficiently good to imply the validity of the USBT requirement that the rear half of the tail fin with decreasing $c(x)$ does not contribute to the linearized yaw dynamics. If this result is general, then it has significant implications for the design of tail fins. The response at $\gamma_0 = -80°$ is shown in Fig. 12(b) to

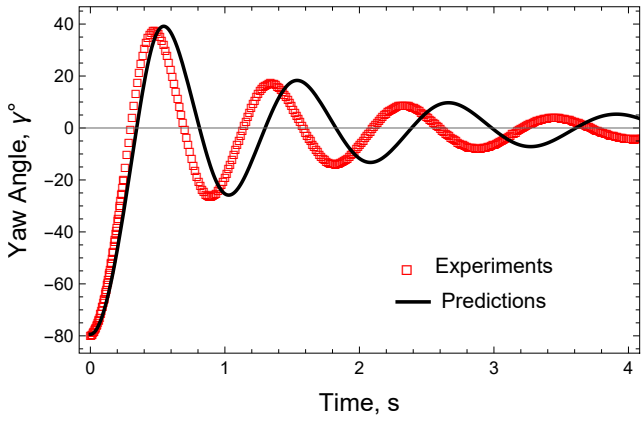

FIG. 10: Yaw angle predictions (black line) compared to the experimental results (□) of a rectangular tail fin of $AR = 0.5, U = 17$ m/s, and $\gamma_0 = -80°$.

be at least as good as for the lower γ_0 in general. The predicted damping is too large. The difference in the frequency response for the two values of γ_0 is difficult to reconcile with the expected superiority of the linear response equations at low $|\gamma|$. It is possible that the difference is a random effect of the incomplete knowledge of the α_i^*s for elliptic planforms.

For the high$-AR$ rectangular tail fin, Fig. 13, the model over-predicts the damping at both release angles. Again, somewhat surprisingly, the errors in the theory are smaller than for the lower AR rectangular fin.

A general observation is that the initial yaw response is predicted accurately for the delta and elliptic fins even when $\gamma_0 = -80°$. From Fig. 5, the high values of γ for small t emphasize the nonlinearity of the response, we conclude that the present model has adequately included the nonlinear effects for those two planforms. The relative poor performance for the rectangular fin shows the need for further refinement of the model constants using system identification as done by Hammam and Wood[9]. This will be the topic for a subsequent publication.

D. Unsteady wind speed

All the moment equations have a term in $\dot{U}$ which has never been tested experimentally. This is probably due to the difficulty in producing a consistent unsteady flow in a wind tunnel, but fortunately we were able to perform experiments with limited, low frequency variations as explained in Section III. The experimental responses were measured at the highest available frequency and amplitude of the approximately sinusoidal variations. Tail fins of the different planforms were tested at different mean wind speed of different amplitudes to cover high and low U. The frequency was $\omega = 0.63$ rad/s, so the wind speed is given by

$$U(t) = U_m + U_a \sin(\omega t + \phi) \tag{16}$$

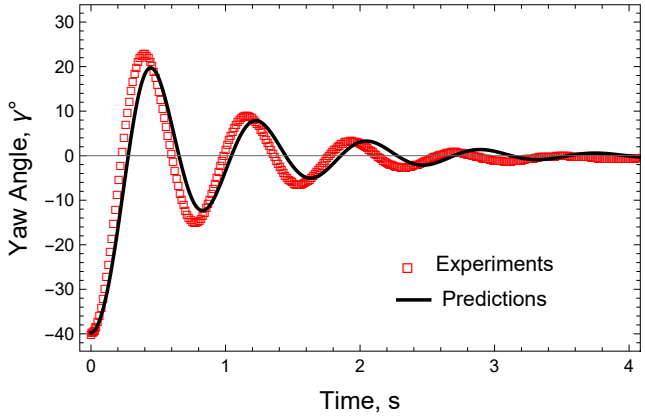

(a) $\gamma_0 = -40°$.

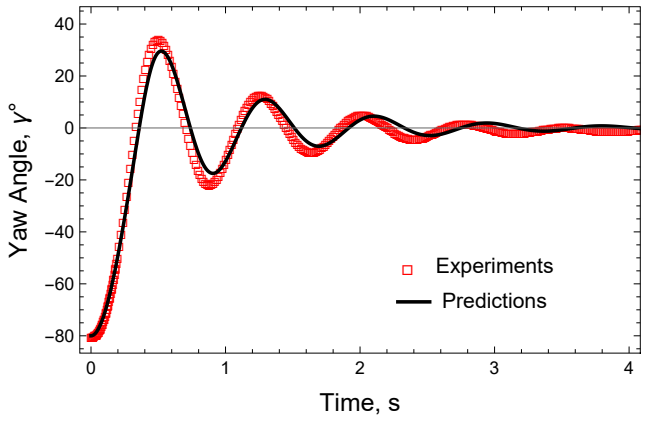

(b) $\gamma_0 = -80°$.

FIG. 11: Yaw angle predictions for a high AR delta tail fin (black line) compared to the experimental results (□). $AR = 1.97, U = 17$ m/s.

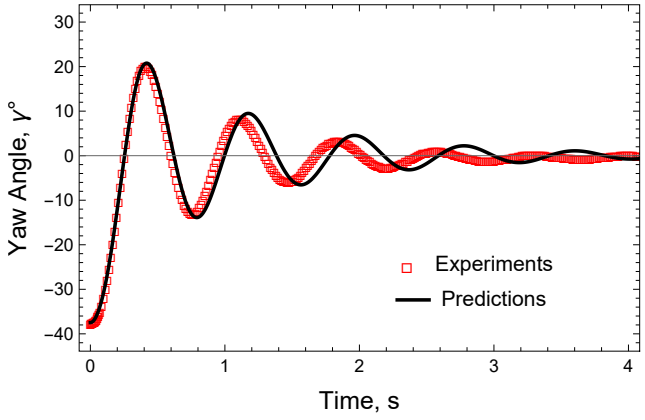

(a) $\gamma_0 = -40°$.

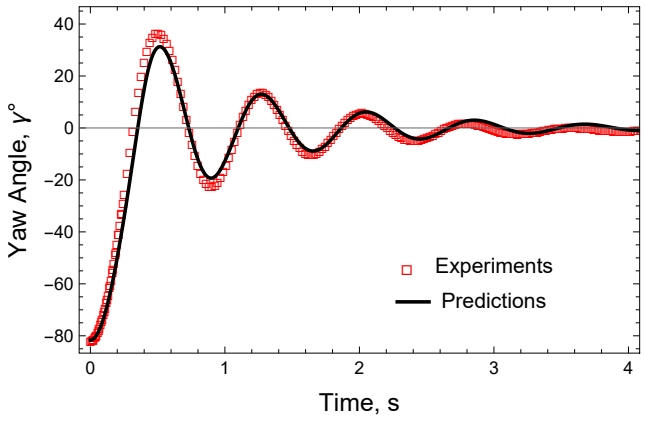

(b) $\gamma_0 = -80°$.

FIG. 12: Yaw angle predictions for an elliptic tail fin (black line) compared to the experimental results (□). $AR = 1.74, U = 17$ m/s.

where $U_m = 9.86$ m/s, $U_a = 1.5$ m/s, the phase angle $\phi = 120°$. Over one cycle of the wind speed variation, the r.m.s. of the difference between the actual wind speed and Eq. (16) was less than 0.16 m/s. The results are shown in Fig. 14 along with the quasi-steady predictions, obtained using Eq. (16) but ignoring the $\dot{U}-$terms in Eq. (1). These are labelled "steady wind". The origin for t in Eq, (16) is also the origin for t in Fig. 14 which shows the response of the delta fin of high AR. It is clear from the figure that the unsteady$-U$ model is no more accurate than the quasi-steady predictions. The same result applied to the other planforms, so these are not shown. It is unlikely that the unsteady$-U$ formulation can be tested in a wind tunnel.

V. LINEARIZING AND OTHER MODIFICATIONS TO THE MODEL

It can be seen from the moment equations for the generic planforms that the yaw response of tail fins is significantly nonlinear for large yaw angles. On the other hand, the yaw responses presented here all have the appearance of a linear, damped, second order system with the nonlinearities confined to the initial response for the higher γ_0 of $-80°$. Linearization is usually achieved by making approximations valid for small γ. This, however, does not result in a fully linear equation because of the $|\sin\gamma|\sin\gamma$ and the $|\sin\gamma|$ terms representing the vortex force, Hammam and Wood[24]. They also showed that a slightly simplified nonlinear equation predicted the response with similar accuracy to the nonlinear equation up to yaw angle of $\gamma_0 = 45°$. At higher angles, the simplified equation deviates considerably from the nonlinear model without the small angle approximation.

One interesting development of the current analysis is to investigate the possibility of a closed form approximation for γ that retains the essential nonlinearity. The authors are currently working on this development.

VI. SUMMARY, CONCLUSIONS, AND RECOMMENDATIONS

The first part of this paper presents and summarizes the derivation of the full, nonlinear yaw moment equations for

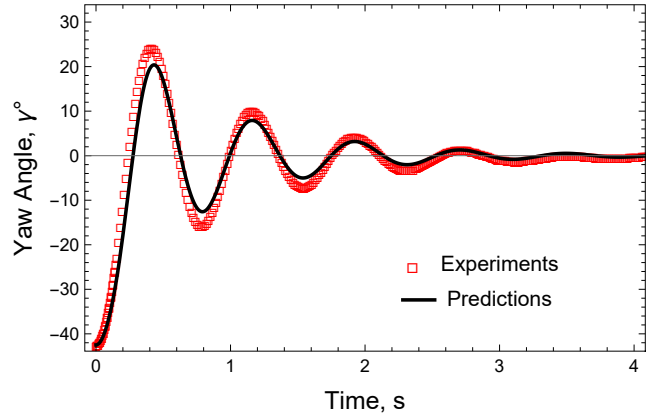

(a) $\gamma_0 = -40°$.

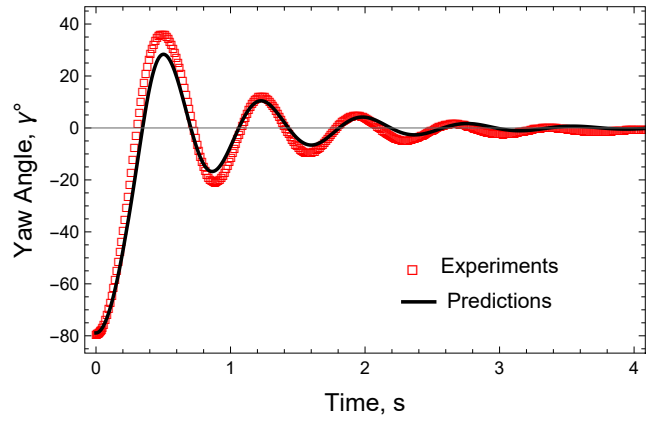

(b) $\gamma_0 = -80°$.

FIG. 13: Yaw angle predictions for a rectangular tail fin (black line) compared to the experimental results (□). $AR = 2.03, U = 17$ m/s.

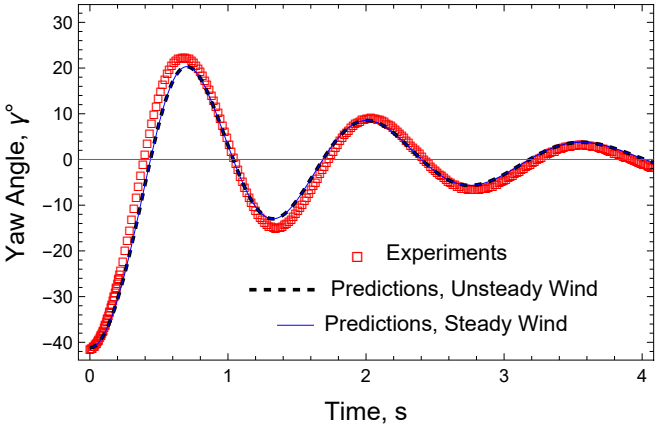

FIG. 14: Yaw angle predictions of the delta fin for unsteady wind speed given by Eq. (16) (black dashed line) and for steady $U = 9.86$ m/s (blue solid line), and the experimental results (□). $AR = 1.97$, $U_m = 9.86$ m/s, $U_a = 1.5$ m/s, $\omega = 0.63$ rad/s, $\phi = 120°$ and $\gamma_0 = -40°$.

a range of generic tail fin planforms for small wind turbines. The equations were derived by Hammam and Wood [9] by starting with unsteady slender body theory (USBT). An extension of USBT to the nonlinear regime is needed for two main reasons. The first is to account for high angles of attack that are most likely to occur when a small wind turbine is starting, and the second is to allow generalization beyond the linearized equations for low aspect ratio generic planforms of delta wings, rectangles, and ellipses. We assume the higher aspect ratio (and more complex planforms) retain the simplification that Reynolds number are negligible. Even for the generic planforms, high aspect ratio was shown to seriously complicate the linear USBT.

In the second part of this paper, we describe measurements of the yaw response of low and high aspect ratio delta wing, elliptical, and rectangular fins with no rotor or nacelle, and the comparison of the results to the full theory.

The linear theory of tail fins and wind vanes is well understood and has some important consequences, Bradney, Evans, and Clausen [4], Singh, Hemmati, and Wood [5], Wood [6], Kerhascoët *et al.* [8]. For example, it is easy to show on dimensional grounds that in the absence of Reynolds number effects, the frequency of response of a tail fin to a change in its yaw angle is proportional to the wind speed at the tail fin. This feature was confirmed by the present experiments which were the first to use a range of wind speeds.

Unsurprisingly, the low angle response is dominated by the "potential flow coefficient" K_p which gives way to the "vortex coefficient" K_v at high angles. K_v was introduced by Polhamus [26] to provide a straightforward model of the effects of the vortices shed from the leading and side edges at high angles. They increment the aerodynamic forces of slender bodies. Additional unsteady effects occur at high angles, such as bursting of the shed vortices, which are modeled in the literature and herein by simple linear differential equations.

The complete equations for the generic planforms at high angles and aspect ratios generally gave good predictions for the wind tunnel experiments with the best accuracy found for the delta tail fins, possibly because it is the only planform for which all constants in our model were available.. The least accurate predictions were for the rectangular planform: the low aspect ratio measurements had a significantly faster response than predicted despite the damping being correctly predicted. Surprisingly, the error in frequency, which occurred only for the elliptic and rectangular planforms, decreased with increasing aspect ratio. Nevertheless, we conclude that USBT provides a good framework to develop tail fin models and to understand the desirable features of them. For example, a tail fin requires a high K_p to track the wind at low angles and only a moderate K_v to avoid high angular velocity at high angles.

ACKNOWLEDGEMENTS

The authors thank Matteo Becchetti from the University of Perugia for his help in wind tunnel experiments. We are also grateful to our NREL colleagues, primarily Jason Jonkman and Brent Summerville, for their many comments and sug-

gestions. The theoretical model was developed by MMH and DHW with funding from the Alliance for Sustainable Energy, LLC, Managing and Operating Contractor for the National Renewable Energy Laboratory for the U.S. Department of Energy. Brent Summerville is the Technical Monitor.

REFERENCES

[1]Https://www.nrel.gov/wind/nwtc/fast.html.

[2]M. Carta, R. Putzu, and T. Ghisu, "A comparison of plunging-and pitching-induced deep dynamic stall on an SD7003 airfoil using URANs and LEs simulations," Aerospace Science and Technology **121**, 107307 (2022).

[3]P. R. Hammer, D. J. Garmann, and M. R. Visbal, "Effect of aspect ratio on finite-wing dynamic stall," AIAA Journal **60**, 6581–6593 (2022).

[4]D. Bradney, S. Evans, and P. Clausen, "The effect of tail fin size on the yaw performance of small wind turbines operating in unsteady flow," in *Colloquium on Research and Innovation on Wind Energy on Exploitation in Urban Environment Colloquium* (Springer, 2018) pp. 55–70.

[5]K. Singh, A. Hemmati, and D. H. Wood, "The aerodynamic characterization of generic tail fin shapes," Wind Engineering **36**, 493–507 (2012).

[6]D. H. Wood, *Small wind turbines: analysis, design, and application* (London: Springer, 2011).

[7]S. Evans, S. Dana, P. Clausen, and D. Wood, "A simple method for modelling fatigue spectra of small wind turbine blades," Wind Energy **24**, 549–557 (2021).

[8]H. Kerhascoët, J. Laurent, A. Cerqueus, M. Sevaux, E. Senn, F. Hauville, and R. Coneau, "Methodology for optimal wind vane design," in *OCEANS 2016-Shanghai* (IEEE, 2016) pp. 1–7.

[9]M. Hammam and D. Wood, "Modeling the yaw behavior of tail fins for small wind turbines," Tech. Rep. NREL-86044 (2023).

[10]E. C. Polhamus, "A concept of the vortex lift of sharp-edge delta wings based on a leading-edge-suction analogy," Tech. Rep. (1966).

[11]L. W. Traub, "Extending slender wing theory to not so slender wings," Journal of Aircraft **40**, 399–402 (2003).

[12]C. Jouannet and P. Krus, "Lift coefficient predictions for delta wing under pitching motions," in *32nd AIAA Fluid Dynamics Conference and Exhibit* (2002) p. 2969.

[13]M. Goman and A. Khrabrov, "State-space representation of aerodynamic characteristics of an aircraft at high angles of attack," Journal of Aircraft **31**, 1109–1115 (1994).

[14]Y. Fan and F. Lutze, "Identification of an unsteady aerodynamic model at high angles of attack," in *21st Atmospheric Flight Mechanics Conference* (1996) p. 3407.

[15]C. Jouannet and P. Krus, "Modelling of high angle of attack aerodynamic," in *25th AIAA Applied Aerodynamics Conference* (2007) p. 4295.

[16]M. V. Lowson and A. J. Riley, "Vortex breakdown control by delta wing geometry," Journal of Aircraft **32**, 832–838 (1995).

[17]M. Okamoto and A. Azuma, "Aerodynamic characteristics at low Reynolds number for wings of various planforms," AIAA Journal **49**, 1135–1150 (2011).

[18]K. Krienes, "The elliptic wing based on the potential theory," Tech. Rep. NACA-TM-971 (1941).

[19]H. Lomax and L. Sluder, "Chordwise and compressibility corrections to slender-wing theory," Tech. Rep. NACA-TR-1105 (1951).

[20]H. B. Helmbold, "Der unvurwundene Ellipsenflügel als tragende Fläche. Report, der Deutschen luftfahrt-forschung," (1942).

[21]J. E. Lamar, "Extension of leading-edge-suction analogy to wings with separated flow around the side edges at subsonic speeds," Tech. Rep. NASA-TR-R-428 (1974).

[22]E. J. Hopkins, "Lift, pitching moment, and span load characteristics of wings at low speed as affected by variations of sweep and aspect ratio," Tech. Rep. NACA-TN-2284 (1951).

[23]F. Castellani, D. Astolfi, M. Becchetti, F. Berno, F. Cianetti, and A. Cetrini, "Experimental and numerical vibrational analysis of a horizontal-axis micro-wind turbine," Energies **11**, 456 (2018).

[24]M. M. Hammam and D. H. Wood, "Aeroelastic modelling of tail fins for small wind turbines," Journal of Physics: Conference Series **2265**, 042073 (2022).

[25]A. Gupta, E. Branlard, M. Hammam, D. Wood, and B. Summerville, "Modeling, implementation and validation of tail fin aerodynamics in openfast," in *NAWEA/WindTECH 2023* (2023).

[26]E. C. Polhamus, "A concept of the vortex lift of sharp-edge delta wings based on a leading-edge-suction analogy," Tech. Rep. NASA TN-D-3767 (1966).